A&A 450, 793–803 (2006)
DOI: 10.1051/0004-6361:20054670

Astronomy & Astrophysics

The effect of the solar wind on CME triggering by magnetic foot point shearing

C. Jacobs, S. Poedts, and B. van der Holst

Centrum voor Plasma-Astrofysica, Celestijnenlaan 200B, 3001 Leuven, Belgium
e-mail: Carla.Jacobs@wis.kuleuven.be

Received 9 December 2005 / Accepted 11 January 2006

ABSTRACT

Context. Photospheric motions and a sheared configuration of the magnetic field are often considered as precursors of violent solar phenomena such as flares and Coronal Mass Ejections (CMEs). Therefore, in many numerical CME initiation studies shearing of the magnetic foot points is used as a mechanism to make the magnetic field unstable and to trigger the CME event.
Aims. From that point of view we decided to do a parameter study that investigates the effect of the different initiation parameters, in particular the effect of the shear flow velocity. Moreover, the simulations were performed on three different background solar wind models. In this way, both effects of the background wind and the initiation parameters on the CME evolution are quantified.
Methods. The results are obtained by means of a finite volume, explicit solver to advance the equations of ideal magnetohydrodynamics. All simulations involve the same numerical grid, the same numerical technique and similar boundary conditions, so that the results can be compared in an unequivocal way.
Results. The foot points of the magnetic field lines are sheared by introducing an extra longitudinal flow profile on the solar surface with a maximum velocity ranging from 3 km s^{-1} to 9 km s^{-1}. The temporal evolution of the magnetic energy, the velocity of the flux rope, and the magnetic helicity show a dependence on the maximum shear velocity as well as on the background wind model.

Key words. Sun: coronal mass ejections (CMEs) – magnetohydrodynamics (MHD) – methods: numerical

1. Introduction

Coronal Mass Ejections (CMEs) belong to the most violent and fascinating events in the solar system. During these dramatic eruptions 10^{12}–10^{13} kg of solar material is ejected into the interplanetary space, releasing energies of typically 10^{25} J (10^{32} erg) on timescales ranging from several minutes to several hours. Typical CME velocities are in the range of 400–500 km s^{-1}, but CME velocities can amount to more than 2000 km s^{-1}. CMEs are a very common phenomenon. Their occurrence rate varies with the solar cycle from one event per week during solar minimum till an average of two to three events per day during solar maximum. These events involve large-scale changes in the coronal structure and significant disturbances in the solar wind. Especially the massive, fast CMEs are interesting to study as these events cause shocks that propagate through the heliosphere, which can, in turn, accelerate energetic particles and cause so-called gradual Solar Energetic Particle (SEP) events. The shocks, energetic particles and magnetic clouds created by CMEs can interact with the magnetosphere of the Earth, where they can cause magnetic storms, which can have pernicious consequences for satellites, communication and navigation systems, power supplies, etc., which promotes CMEs to the most important solar drivers of space weather. Consequently, a careful study of the origin, the structure, and the propagation characteristics of these violent solar phenomena is essential for a deeper insight into basic space weather physics. This, in turn, is required for more accurate and reliable predictions and long-term forecasts of the space weather.

Since the discovery of CMEs in the early seventies, lots of observations have been made and many theories have been developed. Yet, the precise CME triggering mechanism still remains unknown. From observations it is established that CMEs are often associated with flares and prominence eruptions, and that they always originate from closed magnetic field regions on the Sun. Jing et al. (2004) found that 56% of the investigated filament eruptions corresponded with a CME. Gilbert et al. (2000) performed a statistical study of prominence activity and developed definitions of active and eruptive prominences. They came to the conclusion that eruptive prominences are more strongly associated to CMEs (94% of the investigated events) than active prominences (only 46%) and that probably all CMEs associated with eruptive prominences possess

the three-part front-cavity-core structure. As a closed magnetic structure seems to be an important characteristic of CME producing regions on the Sun, it is generally believed that the magnetic field plays an important role in the triggering mechanism for CMEs. Klimchuk (2001) reviewed the different theoretical models for CME initiation and grouped the existing CME models in two major categories, namely "directly driven" models and "storage and release" models. He concluded that all these models have difficulties explaining one or more aspects of the observations. Some examples of CME initiation scenario's are models including shearing of the magnetic foot points (e.g. Steinolfson 1991; Linker & Mikić 1995; Antiochos et al. 1999), models stressing on the emergence of magnetic flux (e.g. Chen & Shibata 2000; Low & Zhang 2002), or models including flux cancellation (e.g. Amari et al. 2000).

In a previous study (Jacobs et al. 2005; Chané et al. 2005) we focussed on the evolution of the CME through interplanetary space. In the present paper, we will focus on the initiation of CMEs, in particular on CME initiation by magnetic foot point shearing. It is well known that prominences are associated with highly sheared magnetic features (Priest et al. 1996). Moreover, shearing motions along the neutral line are often observed before eruptive events and seem to play an important role in these events. Examples of such shear flows can be found in e.g. Yang et al. (2004), who reported the existence of shear flows prior to an X10 flare, or in Romano et al. (2005), who observed a case where a filament eruption was preceded by horizontal, counterclockwise motions in both areas of the filament foot points. From this point of view we decided to investigate which parameters influence the behaviour of sheared arcades. The simulations presented in this paper are based on the work of Linker & Mikić (1995), who did a simulation of the disruption of a helmet streamer by photospheric shear. We extended their study to different models for the background wind and also performed a parameter study in order to investigate the effect of the initiation parameters, such as the shear velocity and the extend of the sheared region, on the evolution of the helmet streamer and the associated CME. All results shown in this paper are 2.5D (i.e. axial-symmetric) and were obtained by solving the equations for ideal Magnetohydrodynamics (MHD) in a numerical way. The numerical technique used to solve the MHD equations is presented in the next section. In the third section, we discuss the different models for the background solar wind, used in the different simulations. The shearing profile is discussed in Sect. 4 and the results of the different simulations are presented in Sect. 5. We end this paper with a discussion of the results and concluding remarks.

2. Numerical technique

The performed computations were done in spherical, axisymmetric (2.5D) geometry described in spherical coordinates (r, θ, φ), where φ is the coordinate in the toroidal direction (in which symmetry is assumed). All simulations are performed with exactly the same grid in the meridional plane, where we used 324 cells in the r-direction and 104 cells in the θ-direction, including 2 ghost cells at each end. The computational domain is restricted to $1-30\ R_\odot$ in the radial direction and covers the region between the north and south pole of the Sun, i.e. $0 \leq \theta \leq \pi$. The computational grid shows a logarithmic accumulation of grid points towards the solar surface, with a grid size varying from $\Delta r = 0.0026\ R_\odot$ at the solar base to $\Delta r = 0.47\ R_\odot$ at the outer boundary (stretch factor $\approx$180), and towards the equator with a grid size varying from $\Delta\theta = 0.0126$ rad at the equator to $\Delta\theta = 0.0629$ rad at the pole (stretch factor $\approx$5). All simulations were performed with a code derived from the Versatile Advection Code (VAC) (Tóth 1996), with the same numerical technique and the same grid. As numerical scheme we chose the Lax-Friedrichs scheme, and the solution is kept divergence free using an approach similar to that of Balsara & Spicer (1999). Instead of storing $(B_r, B_\theta, B_\varphi)$, the magnetic field is stored as vectorpotential component A_φ on the nodal points and B_φ on the cell centres, thereby reducing the number of unknowns in the MHD equations by one. By applying the boundary conditions on A_φ and B_φ, it is therefore also guaranteed that the ghostcell values are divergence free. Furthermore, the description in terms of the vectorpotential A_φ facilitates the computation of the magnetic helicity in Sect. 5.4.

3. Solar wind models

As model for the background solar wind we reconstructed, with the numerical technique described above, three different wind models that are often used in the literature. For every model we used the same initial and boundary conditions and so the only differences between these wind models lies in the physics included in the equations.

The wind models are very similar to the ones described in Jacobs et al. (2005). They are parameterised in the same way, viz. by taking, at the reference position $r_* = 1.01\ R_\odot$, the temperature $T_* = 1.5 \times 10^6$ K, the number density $N_* = 10^8$ cm^{-3}, the angular velocity $\Omega \approx 2.8 \times 10^{-6}$ rad s^{-1}, and the radial component of the magnetic field $B_{r*} = 2.2$ G at the poles, where the magnetic field has initially a dipole configuration. Differential rotation is included in the model in the same way as described in Keppens & Goedbloed (1999). The boundary conditions are very similar to those described in Jacobs et al. (2005), only the boundary conditions at $r = 1$ are slightly modified. At the solar surface the density, temperature, and A_φ are fixed, while the mass flux $r^2\rho v_r$, ρv_θ, and B_φ are left free. The φ-component of the momentum is set to $\rho v_\varphi = \rho\Omega r \sin\theta \pm \rho B_\varphi \sqrt{\frac{v_r^2+v_\theta^2}{B_r^2+B_\theta^2}}$, in that sense we followed the approach of Keppens & Goedbloed (1999) that includes the effect of solar rotation and a coupling with the magnetic field.

The first wind model is the classical polytropic model with polytropic relation: $p = \rho^\gamma/\gamma$, where γ is the ratio of the specific heats and equals 1.05 in our case. This type of wind model was used in many solar wind studies, see e.g. Linker & Mikić (1995); Mikić et al. (1999); Keppens & Goedbloed (1999, 2000); Riley et al. (2001). Because of its simplicity this model is still fairly popular, but it has the drawback of not being able to reproduce the correct ratio of polar versus equatorial wind velocity.

The second model for the solar wind is a reproduction of the model used by Groth et al. (2000) and Manchester et al. (2004). For this wind model, the full set of MHD equations is solved with an additional heating source term of the form

$$Q = \rho q_0 \mathrm{e}^{-\frac{(r-r_0)^2}{\sigma^2}} \left(T_0 - \gamma \frac{p}{\rho} \right),$$

which is added to the energy equation. The ratio of the specific heats for this model is set to $\gamma = 5/3$. The values of T_0 and σ in the heating term are latitude dependent in the same way as described in Manchester et al. (2004) in order to create the regions of fast and slow solar wind. The target temperature T_0 has a value of $T_0 = 2.5 \times 10^6$ K in the region towards the equator below a critical angle $\theta_0(r)$, and a value of $T_0 = 4.375 \times 10^6$ K poleward of the critical angle. The normalized value for q_0 has the same value as in Groth et al. (2000), i.e. $q_0 = 25$, corresponding with a physical value of 1.2×10^6 erg g^{-1} K^{-1} s^{-1}. At the solar surface the critical angle has a value of $\theta_0(r = 1) = 18°$ and there is a smooth transition between the two regions. The heating term has as effect that now a more appropriate ratio between equatorial and polar wind speed is obtained.

In the third solar wind model, the effect of Alfvén wave pressure is included in the same way as, e.g., by Jacques (1978) and Usmanov et al. (2000). In order to include the effect of the Alfvén waves, an extra pressure gradient is added to the momentum equation. We again assume a polytropic relation between density and pressure and take the polytropic index equal to $\gamma = 1.05$, as in the first wind model. Here, however, the extra Alfvén wave pressure has a similar effect as the extra heating term in the second wind model, viz. to yield a more appropriate polar/equatorial velocity ratio. The differences between the three wind models are illustrated in Fig. 1, where the θ- and r-profiles for density and radial velocity are shown at $r = 30\,R_\odot$ and along the equator ($\theta = \pi/2$), respectively.

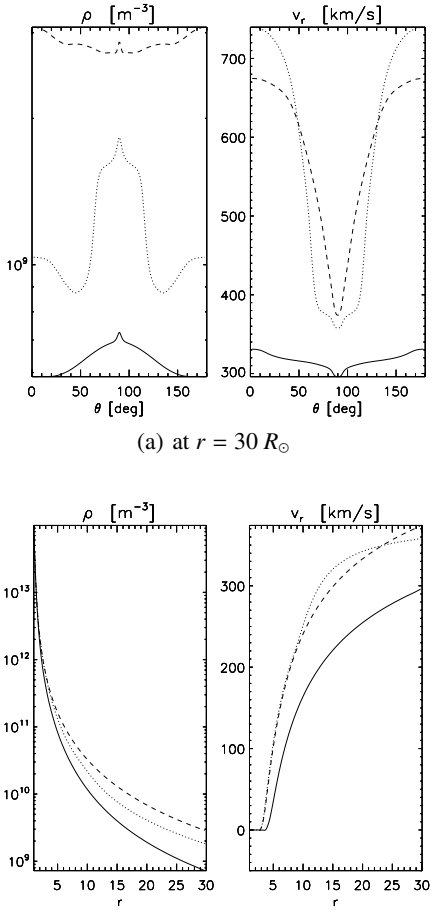

(a) at $r = 30\,R_\odot$

(b) along the equator ($\theta = \pi/2$)

Fig. 1. The profile for density and radial velocity at **a)** 30 $R_\odot$ and **b)** along the equator. Solid line: wind model 1, dotted line: wind model 2, dashed line: wind model 3.

4. Shear flow

The magnetic field in the three axial symmetric solar wind models is up-down symmetric and contains a large helmet streamer across the equator and regions of open magnetic field near the poles. In order to make the helmet streamer unstable, an additional longitudinal velocity is added as a driving source term on the solar surface, in the form of a time-dependent boundary condition. This driving force results in a shearing motion in the magnetic field, causing a swelling of the helmet streamer. The extra longitudinal velocity profile is taken the same as in Mikić & Linker (1994), viz.

$$v_\varphi^0(\theta; t) = v_0(t) \Theta \exp\left[\left(1 - \Theta^4 \right) / 4 \right], \quad (1)$$

where $\Theta = (\theta - 90)/\Delta\theta_m$, with θ the co-latitude in degrees while $\Delta\theta_m$ denotes the width of the shearing profile. In the northern hemisphere the added flow is going in the negative φ-direction, while in the southern hemisphere the extra flow is directed along the positive φ-direction, giving rise to a strong, positive longitudinal component of the magnetic field.

The time dependency of the shearing profile is controlled by the factor $v_0(t)$ in the above formula. The time profile is chosen as follows:

$$v_0(t) = \begin{cases} 0 & \text{if } t \le t_0 \\ v_\varphi^{\max} \frac{1}{2} \left(1 - \cos\left(\pi \frac{t - t_0}{t_1 - t_0} \right) \right) & \text{if } t_0 < t < t_1 \\ v_\varphi^{\max} & \text{if } t_1 \le t. \end{cases}$$

We took $t_0 \approx 12$ h and $t_1 \approx 18$ h. The simulation is stopped after approximately 180 h. As maximum shear velocities we considered values of $v_\varphi^{\max} = 3 - 6 - 9$ km s^{-1}. The value for $\Delta\theta_m$ is at first taken to be 20°, which means that the shearing is maximal at 20 degrees above and below the equator. Simulations where $\Delta\theta_m$ is set equal to 10 and 30 degrees were carried out as well.

5. Results

In response to the imposed shearing of the magnetic foot points the helmet streamer starts rising into the corona and also starts to swell. The shearing increases the outward pointing magnetic pressure force, such that this force is no longer in balance with the inward pointing magnetic tension force and, as a result, an outward expansion can occur. Hence, this process brings

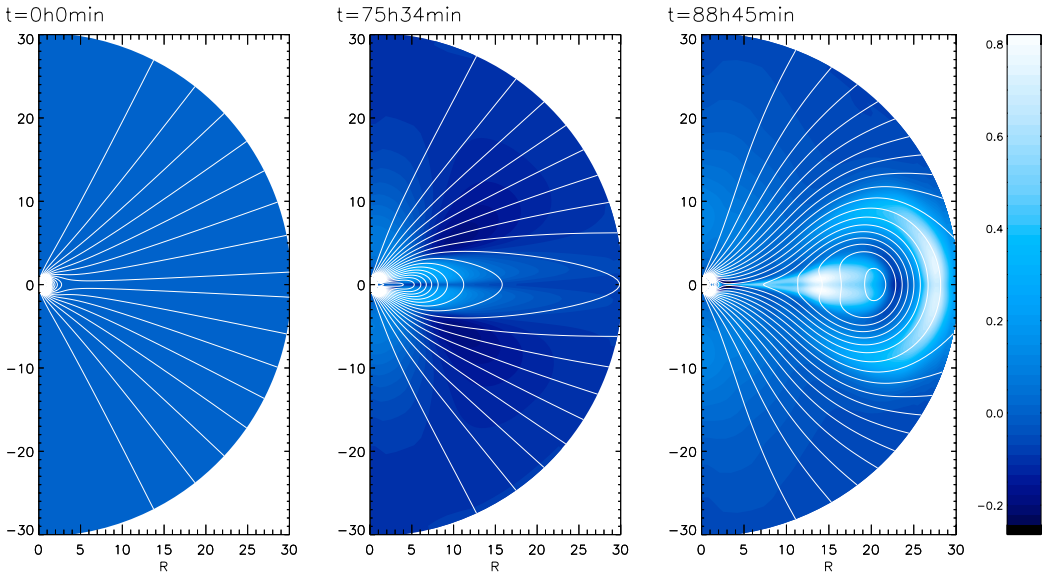

Fig. 2. Three snapshots of the simulation on wind model 1 and $v_\varphi^{\max} = 6\ \mathrm{km\,s^{-1}}$, showing the relative density (colour scale) and the magnetic field lines (white). *On the left*: the stationary wind, *in the middle*: just before the flux rope is formed, *right*: propagation of the flux rope.

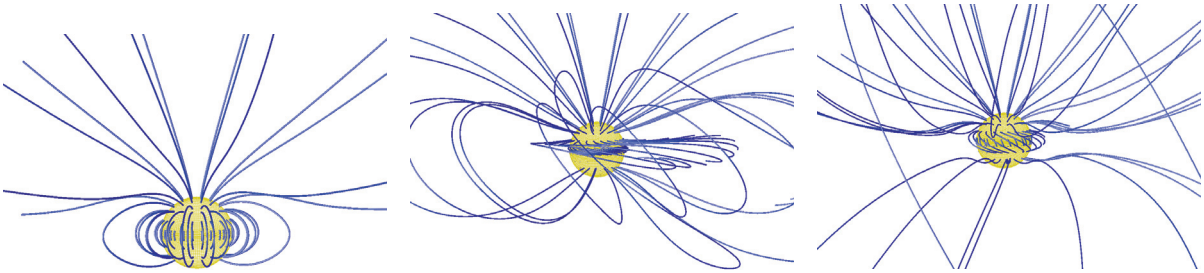

Fig. 3. Representation of the 3D configuration of the magnetic field for the same simulation as in Fig. 2. The snapshots are taken after respectively 0 h, 75 h 34 min and 88 h 45 min.

plasma from the lower corona in the closed field lines region upward, while other plasma is pushed aside by the expanding magnetic field. When the plasma rises into the upper corona it is accelerated by the solar wind and eventually the helmet streamer becomes more and more elongated. At a certain point the evolution becomes catastrophic. A current sheet is formed along the equator and when the thickness of the current sheet becomes small enough, the numerical diffusion becomes important and magnetic reconnection occurs. This magnetic reconnection process causes the formation of a flux rope. The flux rope propagates out of the domain while the reconnection process makes that the helmet streamer is re-built and gets back to its original state. Because the shearing of the foot points is continued, the whole process repeats itself and successive flux ropes are created. In Fig. 2 three snapshots of the simulation with background wind Model 1 and $v_\varphi^{\max} = 6\ \mathrm{km\,s^{-1}}$ are presented. The other simulations behave in a similar way, although there are some exceptions as will be discussed in Sect. 6. What is seen on the figure are the magnetic field lines and the relative density, defined as

$$\bar{\rho} = \frac{\rho_{\mathrm{tot}} - \rho_{\mathrm{w}}}{\rho_{\mathrm{w}}},$$

and expressing the relative amount of extra density with respect to the background wind, where ρ_{w} denotes the density in the stationary wind and ρ_{tot} is the density of the sheared wind. The plot of the relative density $\bar{\rho}$ shows the development of a three-part structure as is often seen in observations: a frontal part with a dense structure, followed by a less dense part ("cavity") that contains the top of the flux rope and than the dense core of the three-part structure.

In Fig. 3 a three-dimensional representation of the magnetic field line configuration is given. The snapshots shown in Fig. 3 correspond to those given in Fig. 2.

5.1. Energetics

A good indication for the formation of the flux rope is the evolution of the magnetic energy W_B of the system. Sheared magnetic fields are stressed and contain an excess of magnetic energy in comparison with the original non-sheared field. Figure 4 shows the evolution of the contribution of the three components of the magnetic field to the magnetic energy for the case of the full MHD wind model (model 2) and a maximum shear velocity of $v_\varphi^{\max} = 6\ \mathrm{km\,s^{-1}}$. For the other simulations performed the evolution of the magnetic energy looks similar. The radial magnetic field component clearly provides the largest contribution to the magnetic energy. In the original non-sheared field, there exists only a minor B_φ-component

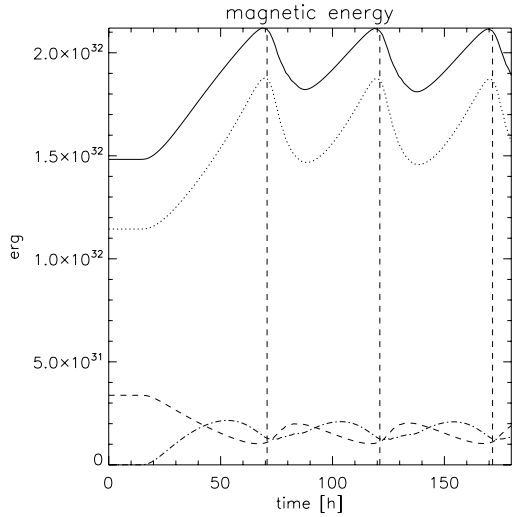

Fig. 4. Evolution of the magnetic energy in time. Solid line: total magnetic energy, dotted line: B_r-contribution, dashed lines: B_θ-contribution, dash-dot line: B_φ-contribution. Background wind model 2 and $v_\varphi^{\max} = 6$ km s^{-1}. The vertical lines denote when the successive flux ropes are formed.

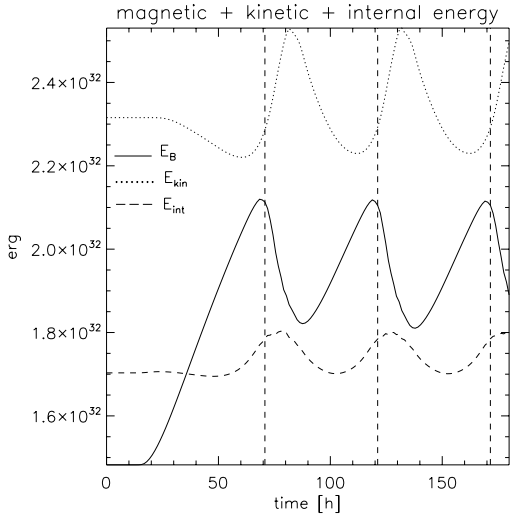

Fig. 5. Evolution of the magnetic (solid), kinetic (dotted) and internal (dashed) energy in time, for the case of background wind model 2 and $v_\varphi^{\max} = 6$ km s^{-1}. The vertical lines denote when the successive flux ropes are formed.

due to the effect of differential rotation, but this component becomes increasingly important to the magnetic energy once the shearing is started. The maximum in W_{B_φ} corresponds to the start of the rapid rise of the streamer, marking the onset of the catastrophic behaviour. When the shearing motions are stopped well before this point, the magnetic field will relax to a new equilibrium, while stopping the shearing motions after this point will result unavoidably in the formation of a flux rope. The vertical lines in Fig. 4 indicate the time of formation of the flux rope, corresponding to a maximum in W_B.

From the moment the magnetic reconnections start, the magnetic energy in the system decreases dramatically and part of the released magnetic energy is converted into internal and kinetic energy (see Fig. 5). The kinetic energy is used to accelerate the newly formed plasmoid, as will be discussed in Sect. 5.2. The amount of magnetic energy released in the first 6 h after the flux rope formation is for all simulations of the order 10^{31} erg, which is a realistic value of energy release in CMEs.

In Fig. 6 the evolution in time of the total magnetic energy is shown and this for different background winds and different values for $v_\varphi^{\max}$. In order to have a uniform normalization, in this figure the magnetic energy is normalized with the amount of magnetic energy in a dipole field $W_{\rm pot}$ with the same flux distribution at the boundary, which is known to be the minimum energy state. As the magnetic field in the stationary background field is partly opened, and thus no longer potential, the magnetic energy of the wind will be slightly higher than the energy in the original dipole. Figure 6 demonstrates that the faster the foot points are sheared, the sooner the flux rope is formed and the higher the peak in magnetic energy is. The chosen model for the background wind also seems to influence the timing and the height of the peak in magnetic energy and, thus, the amount of stored magnetic energy and the time of formation of the flux rope. Also the amount of released magnetic energy is affected by the background wind model. However, the differences are small and when the energy is expressed in physical units these differences in stored and released magnetic energy seem to fade out and the maximum is around 2×10^{32} erg, as can be read from Table 1.

From observations it appears that CMEs involve the transition of a magnetic field configuration from a closed or partly closed configuration to the open state. According to Aly (1984) there is an upper limit to the free magnetic energy that can be stored in the system and released. Sturrock (1991) claimed that this maximum-energy state of a force-free field is the fully-open field configuration. Mikić & Linker (1994) calculated the energy of the fully opened field and found $W_{\rm open} = 1.662 W_{\rm pot}$. Our results are in agreement with the findings of Linker & Mikić (1995), who came to the conclusion that the magnetic energy always remains below $W_{\rm open}$, indicating that this type of simulations do not yield a total opening of the magnetic field. The issue whether or not all the magnetic field opens, still has to be resolved observationally and can be a constraint for theoretical CME models.

From the energy equation the amount of dissipated energy can be computed. As the gradients in the second wind model are the steepest, the simulations on this wind model will suffer the highest numerical dissipation. This is because the finite volume method reduces from second to first order there where the gradients are too steep. This gives an upper boundary for the global dissipation of -10^{30} erg h^{-1}, or when expressed in terms of the total energy in the background wind: 0.5% of the background wind energy is dissipated per hour as a result of numerical dissipation.

5.2. Velocity

The velocity at which the centre of the flux rope propagates through interplanetary space also depends on the shear velocity and as well on the background wind model. For the

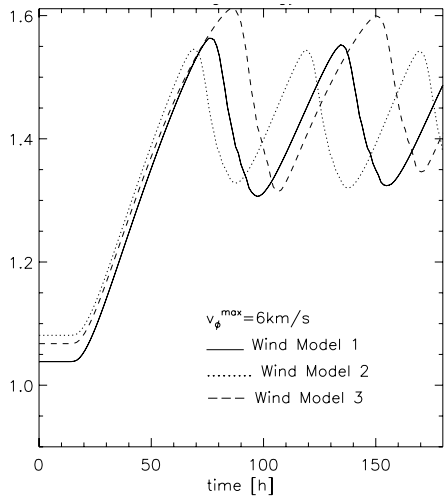

(a)

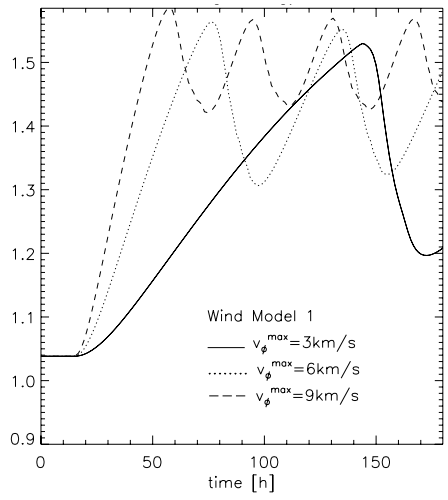

(b)

Fig. 6. Evolution of the magnetic energy in time. **a)** Evolution of the magnetic energy in the three different background wind models with $v_\varphi^{\max} = 6\ \mathrm{km\,s^{-1}}$. **b)** Evolution of the magnetic energy for different shearing velocities, but with the same background wind model (Model 1).

effect on the velocity we refer to Fig. 7. As the three different wind models have different velocities along the equator (see Fig. 1b), the differences in flux rope speed for the different winds are an expected result. For the same wind model but different values of $v_\varphi^{\max}$, however, the different velocities are obtained due to a more or less effective transformation of magnetic to kinetic energy. For example, for the first wind model and $v_\varphi^{\max} = 9\ \mathrm{km\,s^{-1}}$ 85% of the magnetic energy is converted to kinetic energy during the first 6 h after the flux rope formation, while it is only 50% in the case of $v_\varphi^{\max} = 3\ \mathrm{km\,s^{-1}}$. The average velocity is estimated as the slope of the straight line fitted through the curve giving the position of centre of the flux rope in time and the values can be found in Table 1. The velocity of the flux rope lies within the range of 300–400 $\mathrm{km\,s^{-1}}$ and can be classified as a slow CME event. The flux rope is first accelerated and will finally propagate with the same speed as the background wind. As average acceleration we find values

Table 1. Overview of some results for the different simulations ($\Delta\theta_m = 20°$). The table contains information about the moment when for the first time a flux rope appears in the simulation, the time interval between the successive flux ropes, the maximum amount of shear of the solar surface when the flux rope is formed, the average velocity of the centre of the propagating flux rope and the maximum value in magnetic energy. Bold numbers indicate values that are not in the expected range.

$v_\phi^{\max}$	Model 1	Model 2	Model 3
Approximate time formation 1st flux rope (FR)			
3	147 h	–	**238 h**
6	77 h	70 h	87 h
9	58 h	53 h	62 h
Time interval between FR's			
3	–	–	–
6	58 h	50 h	64 h
9	36 h	34 h	37 h
Amount of sheared solar surface			
3	65%	-	**110**%
6	62%	55%	71%
9	64%	57%	69%
Average velocity FR [$\mathrm{km\,s^{-1}}$]			
3	301	–	301
6	327	368	334
9	339	374	350
Maximum in magnetic energy [10^{32} erg]			
3	2.09	2.03	2.16
6	2.13	2.12	2.21
9	2.16	2.15	2.24

of 2–3 $\mathrm{m\,s^{-2}}$, which is comparable to the observations (Yashiro et al. 2004; Vršnak et al. 2004).

5.3. Width of the shearing region

Broadening or narrowing the width of the shearing profile has also an influence on the behaviour of the flux rope formation. When the width of the shearing region is lowered to a value of 10°, then no flux rope is formed at all, not even when the simulation is extended until a time $t_{\max} \approx 360$ h. The helmet streamer does elongate in this case, but it does not swell like in the simulations with $\Delta\theta_m = 20°$. For the case of the polytropic wind model (model 1) and $v_\varphi^{\max} = 6\ \mathrm{km\,s^{-1}}$ the magnetic energy reached its maximum value (2.09×10^{32} erg) at time $t \approx 315$ h, followed by a sudden decrease in magnetic energy, indicating that the reconnection process has started. However, this does not result in the formation of a flux rope like the one shown in Fig. 2. Broadening the profile to 30°, on the other hand, does still yield the formation of a flux rope. However, it is formed at ≈67 h, which is earlier than for the $\Delta\theta_m = 20°$ case. The maximum in magnetic energy now amounts to 2.08×10^{32} erg.

These differences with the case of $\Delta\theta_m = 20°$ are to be expected and due to the extend of the closed field line region. In the case of the narrower profile, there are more closed field lines lying above the sheared arcade, preventing the arcade to erupt,

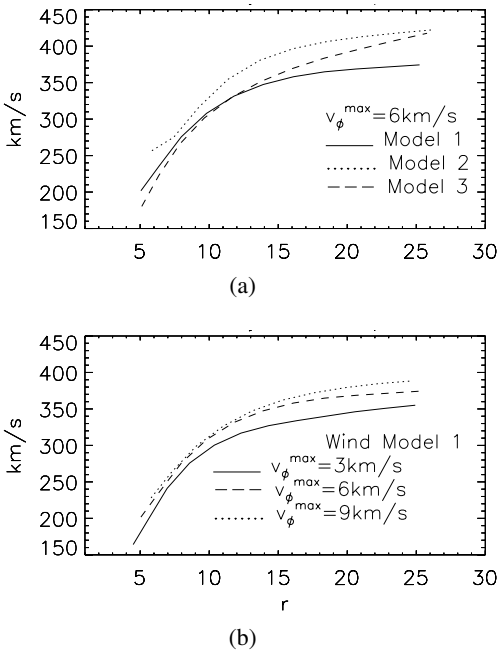

Fig. 7. The velocity of the centre of the flux rope. **a)** $v_\varphi^{\max} = 6\ \mathrm{km\,s^{-1}}$, three different models for the background wind. **b)** Three different shear velocities, background wind model is Model 1.

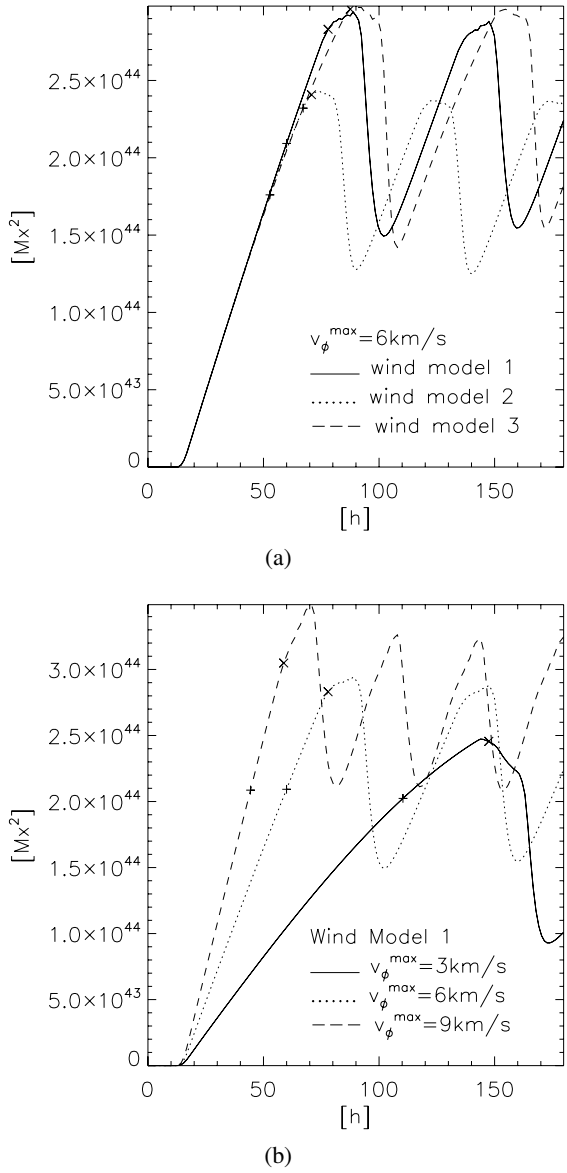

Fig. 8. Evolution in time of the total helicity in the simulation volume. **a)** Three different wind models, $v_\varphi^{\max} = 6\ \mathrm{km\,s^{-1}}$. **b)** Three different shear velocities (wind model 1). The +−signs indicate the beginning of the dramatic rise of the streamer. The formation of the flux rope is marked by the ×-symbol.

while for the broader profile the complete helmet streamer is sheared and the plasmoid is formed faster.

5.4. Magnetic helicity

Helical structures or helical-like patterns are often observed during filament eruptions and CMEs. Therefore, a general opinion is that the helicity of the involved magnetic fields appears to hold an important key to the onset of solar eruptions such as flares and CMEs. Observational studies of the helicity budget of active regions and the amount of helicity carried away by CMEs is reported by many authors (e.g. DeVore 2000; Chae 2001; Démoulin et al. 2002; Démoulin & Berger 2003; Nindos & Zhang 2002; Nindos et al. 2003) and the possible relation between the helicity injection rate and the occurrence of eruptive events is also a popular research subject (e.g. Moon et al. 2002; Chae et al. 2004; Nindos & Andrews 2004; Romano et al. 2003, 2005). As we have the advantage of knowing the magnetic field components and the longitudinal component of the vector potential on the entire computational domain, it may be interesting to compute the helicity budget in the different simulations we performed.

The formula for the relative magnetic helicity, which is a gauge invariant expression, is given by (Berger 1988):

$$H_r = \int_V (\boldsymbol{A} + \boldsymbol{A}_\mathrm{p}) \cdot (\boldsymbol{B} - \boldsymbol{B}_\mathrm{p}) \mathrm{d}V, \tag{2}$$

where $\boldsymbol{B}$ is the magnetic field, $\boldsymbol{A}$ is the magnetic vector potential, $\boldsymbol{B}_\mathrm{p}$ denotes the potential magnetic field that has the same flux distribution as $\boldsymbol{B}$ on the boundary ($\boldsymbol{B}_\mathrm{p}.\boldsymbol{n}|_S = \boldsymbol{B}\cdot\boldsymbol{n}|_S$), and $\boldsymbol{A}_\mathrm{p}$ is the vector potential corresponding to $\boldsymbol{B}_\mathrm{p}$. In the case of axial-symmetry, the vector potential $\boldsymbol{A}_\mathrm{p}$ can be chosen such that $\boldsymbol{A}_\mathrm{p} = (0, 0, A_\mathrm{p})$ and on the boundary the relation $A_\varphi|_S = A_\mathrm{p}|_S$ is satisfied. According to Antiochos et al. (2002) the formula for relative helicity then simplifies to:

$$H_r = 2 \int_V A_\varphi B_\varphi \mathrm{d}V, \tag{3}$$

where the longitudinal component of the magnetic vector potential A_φ is a known value because of the chosen numerical method (it is one of the dependent variables in our modified version of the VAC code). A plot of the evolution in time of the total amount of relative helicity in the simulation volume is given in Fig. 8. Values for the total amount of relative helicity at the moment of the beginning of the dramatic rise of the streamer (maximum in W_{B_φ}) and at the moment of flux rope

Table 2. Values concerning the helicity budget for the different simulations ($\Delta\theta_m = 20°$). Shown are the values for the amount of helicity in the total simulation volume and the amount of helicity injected through the solar surface, both at the moment when the instability sets in and when the flux rope is formed. Also listed is the amount of helicity transported by the flux rope through the outer boundary. The numbers in bold indicate values that are not in the expected range.

$v_\phi^{\max}$	Model 1	Model 2	Model 3
Amount of relative helicity in the volume $[H/\Phi^2]$			
At time of onset instability			
3	0.18	–	0.20
6	0.19	0.16	0.21
9	0.19	0.16	0.20
At time of FR formation			
3	0.22	–	0.22
6	0.25	0.21	0.26
9	0.27	0.24	0.28
Amount of helicity injected $[H/\Phi^2]$			
At time of onset instability			
3	0.21	–	**0.30**
6	0.20	0.16	0.23
9	0.19	0.16	0.21
At time of FR formation			
3	0.28	–	**0.48**
6	0.27	0.24	0.31
9	0.28	0.25	0.31
Amount of helicity carried away by plasmoid $[10^{44}\ \mathrm{Mx}^2]$			
3	–1.49	–	–1.20
6	–2.03	–1.57	–1.54
9	–2.44	–2.11	–2.07

formation are given in Table 2, and are indicated on Fig. 8 with +−signs and ×-signs, respectively.

However, the amount of coronal helicity is difficult to determine from observational data. A more common, observationally reported, quantity is the "helicity injection rate". As our simulation is axial-symmetric, $\boldsymbol{A}_\mathrm{p}$ satisfies the conditions $\nabla \cdot \boldsymbol{A}_\mathrm{p} = 0$ and $\boldsymbol{A}_\mathrm{p} \cdot \boldsymbol{n}|_S = 0$. The total time derivative of the relative helicity, in case of ideal MHD, can then be expressed as (Berger 1999):

$$\frac{\mathrm{d}H_r}{\mathrm{d}t} = 2 \oint_S \left[\left(\boldsymbol{A}_\mathrm{p} \cdot \boldsymbol{v} \right) \boldsymbol{B} - \left(\boldsymbol{A}_\mathrm{p} \cdot \boldsymbol{B} \right) \boldsymbol{v} \right] \mathrm{d}\boldsymbol{S}, \tag{4}$$

which simplifies, in our specific case, to:

$$\frac{\mathrm{d}H_r}{\mathrm{d}t} = 2 \oint_S \left[\left(A_\varphi v_\varphi \right) \boldsymbol{B} - \left(A_\varphi B_\varphi \right) \boldsymbol{v} \right] \mathrm{d}\boldsymbol{S}. \tag{5}$$

The two terms on the right-hand side express the change of helicity by shearing motions and magnetic flux emergence, respectively. It is clear that for the kind of simulations reported on here, the first term in Eq. (5) is the most important one at the inner boundary of the computational domain, while at the outer boundary the largest contribution will come from the second term because of the presence of the background wind. The amount of helicity in the stationary wind equals zero, so there is no contribution of the differential rotation. This is because for the generation of the wind models we initially started from a dipole configuration for the magnetic field (which has zero helicity), and during the evolution towards the steady wind there is no helicity injected through the boundaries, as at the boundaries the profiles for A_φ, v_φ and v_r are symmetric and B_r and B_φ are anti-symmetric so that both terms in the RHS of Eq. (5) will be zero. In Fig. 9 the amount of helicity injected through the lower boundary (during the application of the shearing boundary condition) is plotted versus time. The beginning of the dramatic rise and the moment of flux rope formation are again indicated with +−signs and ×-signs. More information about the values of the injected helicity can be found in Table 2.

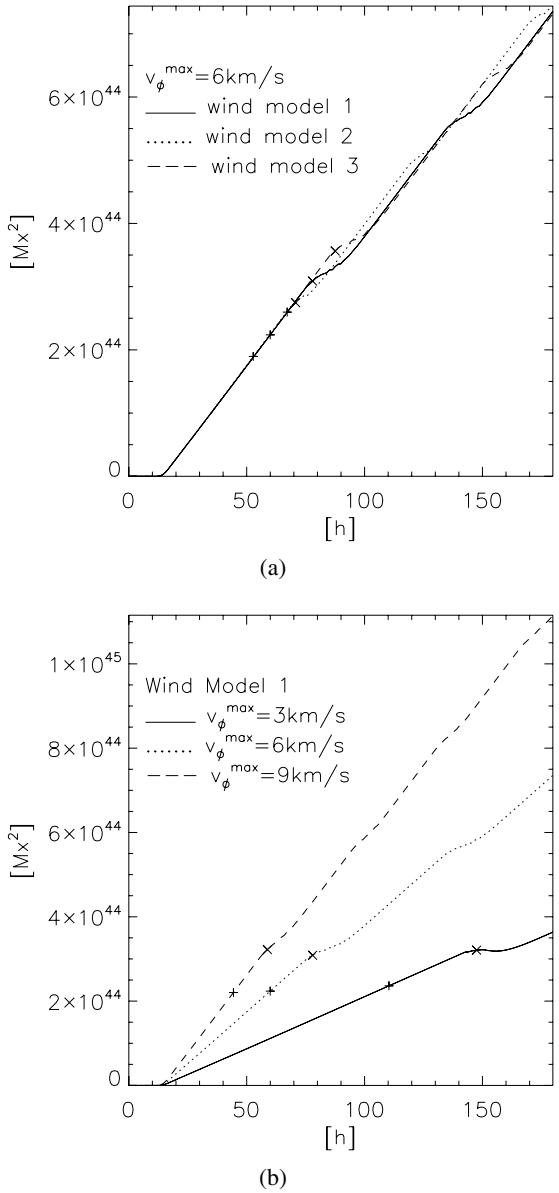

Fig. 9. Evolution in time of the amount of injected helicity through the lower boundary. **a)** Three different wind models, $v_\varphi^{\max} = 6\ \mathrm{km\,s^{-1}}$. **b)** Three different shear velocities (wind model 1). The +−signs indicate the beginning of the dramatic rise of the streamer. The formation of the flux rope is marked by the ×-symbol.

As the shearing starts only after $t = t_0 \approx 12$ h, during the first 12 h of the simulation there will be no helicity injected (see Figs. 8 and 9) through the lower boundary. Because the shearing is a continuous process, after $t = t_0$ helicity is uninterruptedly injected in the coronal volume. When looking at the positions of the symbols indicating the onset of the instability and the formation of the flux rope in Fig. 9 it seems that the amount of helicity to be injected into the corona to create the flux rope does depend on the used model for the background wind (Fig. 9a), but that within the same wind model it is more or less independent of the applied shear velocity (Fig. 9b). This can also be derived from the values mentioned in Table 2. Figure 8b shows that at the start of the dramatic rise of the streamer the helicity in the coronal volume is approximately the same for the three different shearing velocities, but that this is not the case when the flux rope is formed. This is because the rise of the field lines that proceeds the flux rope formation takes longer when the shearing is slower, and so more closed field lines are able to reach the outer boundary, before the flux rope arrives. The sudden decrease in helicity in Figs. 8a and 8b corresponds with the passage of the flux rope through the outer boundary, and so the CME carries away part of the helicity in the simulation volume. The passing of the flux rope is marked by a sudden rise in poloidal flux $\psi = r \sin\theta A_\varphi$. This enables us to estimate the amount of magnetic helicity carried away by the CME. The values are summarised in Table 2 and are of the order 10^{44} Mx^2, which is rather high in comparison with the observations of the amount of helicity in magnetic clouds. However, this is due to the fact that the present simulations are performed in an axi-symmetric model, which means that the shearing region goes all the way around the solar surface instead of just a few degrees, yielding an over-estimation by a factor of at least 100. The simulations show that the amount of helicity in the flux rope depends on the applied background wind model as well as on the shearing velocity.

6. Discussion

Table 1 gives an overview of the characteristics of the different simulations, such as the moment when the first flux rope appeared in the domain during the simulation, the time interval between the successive flux ropes, and the propagation velocity of the flux rope. In Table 2 some values concerning the helicity budget are listed for the different simulations.

After the formation of the first flux rope the newly created helmet streamer will start swelling again due to the constant shear flow at the boundary and the process of flux rope formation repeats on and on till the end of the simulation. The time interval between the successive flux ropes formed in one simulation stays constant and scales more or less inversely proportional to the maximum shear velocity: the faster the shearing the faster the flux ropes follow each other. Values for these time intervals are listed in Table 1. Assuming that the magnetic foot points follow the shear flow exactly, the amount of solar surface that has to be sheared before a flux rope forms can be computed (see Table 1). This leads us to the conclusion that the process of flux rope formation does depend on the chosen model for the background wind. Moreover, we can conclude that it is the accumulative amount of shear and not the shearing velocity that is important for the formation of the plasmoid, as also reported by Mikić & Linker (1994). However, there are some exceptions as gathered from Table 1, namely the simulations with $v_\varphi^{\max} = 3$ km s^{-1} and background wind model 2 and model 3. In the case of model 3 there was no flux rope formed during the first 180 h of the simulation. When extending the shearing time until $t_{\max} \approx 300$ h, the simulation indeed showed the expected dramatic rise of the streamer and the formation of a plasmoid, but the amount of shear necessary to get this effect is much larger in this case than in the other simulations with wind model 3. In the case of solar wind model 2, the catastrophic behaviour never occurred for $v_\varphi^{\max} = 3$ km s^{-1}, not even when extending the simulation until more than $t_{\max} \approx 300$ h. The helmet streamer does elongate in this case, just like in the other simulations, but it does not swell that much. A reconnection event does occur, but it is much less violent than in the other simulations. Hence, the magnetic reconnection event does not create a flux rope in this case, and the reconnection site is situated higher up in the corona, indicating that this reconnection may be a numerical artefact due to the relatively high numerical dissipation as mentioned in Sect. 5.1. The numerical dissipation causes a slippage of the field lines (Steinolfson 1991; Mikić et al. 1988; Mikić & Linker 1994), such that the field lines do not follow the longitudinal flow exactly. This makes us conclude that in the case of background wind model 1 the minimum driving velocity of $v_\varphi^{\max} = 3$ km s^{-1} is sufficiently far above the slippage velocity, as the formation of the plasmoid only seems to depend on the amount of shear and not on the shearing velocity. In case of the third wind model the minimum shear velocity is approximately equal to the slippage velocity, while for the second wind model it is lower than the slippage velocity. This also means that decreasing the numerical dissipation, so decreasing the slippage velocity, should solve the problem. As a matter of fact, the same simulation on a grid with double resolution in both $r-$ and $\theta-$direction (i.e., with 644×204 grid cells) results in the formation of a flux rope in the second wind model for $v_\varphi^{\max} = 3$ km s^{-1}. The flux rope is then formed after ≈110 h, which is somewhat earlier than the expected ≈122 h, when analysing the results for $v_\varphi^{\max} = 6$ and 9 km s^{-1} on the low resolution wind. The reason is that the slippage velocity is now smaller, and so the amount of critical shear is reached sooner. We thus also repeated the simulation with wind model 1 and $v_\varphi^{\max} = 6$ km s^{-1} with the same higher resolution grid. This simulation shows a similar effect, but it is less pronounced in this case. The flux rope is now formed after ≈75 h, which is slightly faster than the 77 h obtained with the lower resolution grid. When the numerical dissipation is reduced, the magnetic field can build up more energy before it starts to reconnect, and so the resulting flux rope propagates at a slightly higher velocity. We found average velocities of 363 km s^{-1} (model 1, $v_\varphi^{\max} = 6$ km s^{-1}) and 368 km s^{-1} (model 2, $v_\varphi^{\max} = 3$ km s^{-1}), which is higher, but still in the range of the velocities obtained with the lower resolution grid.

Table 1 also lists numbers for the maximum value of the magnetic energy. The evolution of the magnetic energy was discussed in Sect. 5.1. Whitin the simulations on the same wind

model, the biggest difference in magnetic energy occurs for wind model 2. In the case of $v_\varphi^{\max} = 3\ \mathrm{km\,s^{-1}}$ the maximum in magnetic energy is rather low compared to the other values. Increasing the resolution yields a higher peak in magnetic energy: in case of wind model 2 and $v_\varphi^{\max} = 3\ \mathrm{km\,s^{-1}}$ it is shifted to 2.13×10^{32} erg and for wind model 1 and $v_\varphi^{\max} = 6\ \mathrm{km\,s^{-1}}$ it is changed to 2.17×10^{32} erg.

The fact that it is the amount of shearing of the magnetic field lines and not the shear velocity that is the driving factor for the instability can also be derived from Table 2. Here we listed the amount of helicity in the total volume of the computational domain and the amount of helicity injected through the photosphere, expressed as the square of the amount of total magnetic flux (Φ^2) through the lower boundary, in order to be able to compare our results with the ones reported in the related literature. As we keep the magnetic flux fixed, it is the same for all simulations, viz. $\Phi = 3.36 \times 10^{22}$ Mx. The expression for the total helicity (Eq. (3)) is independent of the shear velocity, in contrast to expression (5), and so Eq. (3) only takes into account the shear in the magnetic field. We conclude from the values listed in Table 2 that the total amount of helicity in the coronal volume is a more important criterion for the onset of the instability than the amount of injected helicity. For example in wind model 3 and $v_\varphi^{\max} = 3\ \mathrm{km\,s^{-1}}$, the flux rope is formed much later, as explained earlier, and so the amount of injected helicity will be much larger than for the other simulations on wind model 3. However, at the moment of the onset of the instability, the amount of helicity in the coronal volume has approximately the same value as for the other two cases. For the simulation on wind model 2 and $v_\varphi^{\max} = 3\ \mathrm{km\,s^{-1}}$ we experience the same. During the complete simulation ($t_{\max} \approx 180$ h) the total amount of helicity reached a maximum value of $H/\Phi^2 = 0.16$, the value for the onset of the instability, but this value was never exceeded, and no flux rope was formed for this simulation. For the simulation where the extend of the shearing region was reduced to $\Delta\theta_m = 10°$, the coronal helicity measured a maximum value of $H/\Phi^2 = 0.18$, and, again, there was no flux rope formed in this simulation. The conclusion from these observations is that, in order to force the formation of a flux rope, the value of the coronal magnetic helicity should sufficiently exceed the critical value.

The values we obtained for the coronal helicity and the helicity carried away by the plasmoid are much higher than the values reported from observations. Typical values for helicity found in literature are of the order 10^{42} Mx^2, while what we find is two orders of magnitude larger. This can be explained by the fact that we integrated over the entire solar surface, while observational reports only consider one active region. Moreover, it should be mentioned that helicity computations from observations are susceptible to many assumptions and probably underestimate the amount of helicity (van Driel-Gesztelyi et al. 2003). When we express the helicity in the more "natural" units of Φ^2 our results are better comparable with those reported in the related literature. Démoulin et al. (2002) mention that for the case they investigated, the maximum coronal helicity is in the interval $\approx[0.2, 0.3]$. van Driel-Gesztelyi et al. (2003) listed an overview of the amount of injected helicity by photospheric shear for different active regions and they mention values in the range $[0.003, 0.2]$ where the maximum observing time never exceeded 120 h. Nindos & Zhang (2002) believe that horizontal motions cannot produce enough helicity to provide the helicity ejected into the interplanetary medium. This may also be an explanation for the high helicity in our simulations, because we had to give the magnetic foot points an unrealistic amount of shear before the flux rope was formed, and so we added more helicity by shearing motions than in the real sun.

7. Conclusions

Shearing of the magnetic field lines is indeed a mechanism to make the helmet streamer magnetic field unstable and to trigger a CME, like already shown by Linker & Mikić (1995). The extensive parameter study that we performed showed that the applied model for the background wind in these simulations does influence the results. The differences in density and velocity of the background wind affect the instability threshold and make it different for the three different solar winds. It also influences the resulting velocity of the propagating flux rope. Also the maximum velocity at which the magnetic foot points are sheared and the width of the shear region have affected the results. The faster the shearing, the faster the instability in the magnetic field will occur, but also the more efficient the conversion of magnetic to kinetic energy and, as a consequence, the faster the flux rope propagates. The wider the shearing region, the easier the flux rope can be formed, while for a too narrow shearing region, the tension force of the overlying field prohibits the formation of a flux rope. Another important conclusion is that the total relative helicity seems to play an important role in the onset of the instability. However, we cannot conclude from our parameter study that this is the only factor that determines whether a CME will be formed or not, as the helicity threshold is different for the different wind models. Phillips et al. (2005) did a numerical simulation of CME triggering using the "break-out-model" (Antiochos et al. 1999) where they showed that the eruption occurred at a fixed magnitude of free energy in the corona, independent of the value of the helicity, and so that helicity does not play a determining role in CME initiation. We believe that both helicity and magnetic energy are important players in the CME triggering mechanism. From the results presented in Sect. 5 it can be concluded that the magnetic energy at the moment of eruption depends on the shear velocity and the wind model as well as on the width of the shear region, but the differences are small. When there is no reconnection event, the magnetic energy is indeed less than for the simulations resulting in the formation of a flux rope.

The drawback of this axi-symmetric model is that it is not able to create fast CMEs. Moreover, the amount of shear to be added in order to make the magnetic field unstable is unrealistically high, and so is the required shear velocity. The minimum peak velocity we considered was $3\ \mathrm{km\,s^{-1}}$, while in literature velocities of one order less are mentioned for the photospheric motions (e.g. Romano et al. 2005). The high numerical dissipation of the Lax-Friedrichs scheme did not allow us to take lower values for the driving velocity. Observations show that it are

not only shearing motions, but also flux emergence that seems to be important in the onset mechanism of CMEs. Finally, the sun is not a 2.5D object. The magnetic field has clearly a fully 3D configuration. Therefore, extending this work to 3D models for the solar wind, and to improve the CME initiation models to models where shearing of magnetic field lines and emerging of magnetic flux are combined is one of the aims of our future work.

Acknowledgements. These results were obtained in the framework of the projects GOA 2004/01 (K.U.Leuven), 90203 (ESA Prodex 8), and G.0451.05 (FWO-Vlaanderen).

References

Aly, J. J. 1984, ApJ, 283, 349
Amari, T., Luciani, J. F., Mikić, Z., & Linker, J. A. 2000, ApJ, 529, L49
Antiochos, S., DeVore, C., & Klimchuk, J. 1999, ApJ, 510, 485
Antiochos, S., Karpen, J., & DeVore, C. 2002, ApJ, 575, 578
Balsara, D. S., & Spicer, D. S. 1999, J. Comp. Phys., 149, 270
Berger, M. A. 1988, A&A, 201, 355
Berger, M. A. 1999, Plasma Phys. Controlled Fusion, 41, B167
Chae, J. 2001, ApJ, 560, L95
Chae, J., Moon, Y.-J., & Park, Y.-D. 2004, Sol. Phys., 223, 39
Chané, E., Jacobs, C., van der Holst, B., Poedts, S., & Kimpe, D. 2005, A&A, 432, 331
Chen, P., & Shibata, K. 2000, ApJ, 545, 524
Démoulin, P., & Berger, M. A. 2003, Sol. Phys., 215, 203
Démoulin, P., Mandrini, C. H., van Driel-Gesztelyi, L., et al. 2002, A&A, 382, 650
DeVore, C. R. 2000, ApJ, 539, 944
Gilbert, H. R., Holzer, T. E., Burkepile, J. T., & Hundhausen, A. J. 2000, ApJ, 537, 503
Groth, C. P. T., De Zeeuw, D. L., Gombosi, T. I., & Powell, K. G. 2000, J. Geophys. Res., 105, 25053
Jacobs, C., Poedts, S., van der Holst, B., & Chané, E. 2005, A&A, 430, 1099
Jacques, S. A. 1978, ApJ, 226, 632
Jing, J., Yurchyshyn, V. B., Yang, G., Xu, Y., & Wang, H. 2004, ApJ, 614, 1054
Keppens, R., & Goedbloed, J. P. 1999, A&A, 343, 251
Keppens, R., & Goedbloed, J. P. 2000, ApJ, 530, 1036
Klimchuk, J. A. 2001, in Geophys. Monograph Series, Space Weather, ed. P. Song, H. J. Singer, & G. L. Siscoe (AGU), 125, 143
Linker, J., & Mikić, Z. 1995, ApJ, 438, L45
Low, B., & Zhang, M. 2002, ApJ, 564, L53
Manchester, W., Gombosi, T., Roussev, I., et al. 2004, J. Geophys. Res., 109, A01102
Mikić, Z., & Linker, J. 1994, ApJ, 430, 898
Mikić, Z., Barnes, D. C., & Schnack, D. D. 1988, ApJ, 328, 830
Mikić, Z., Linker, J. A., Schnack, D. D., Lionello, R., & Tarditi, A. 1999, Phys. Plas., 6, 2217
Moon, Y.-J., Chae, J., Choe, G. S., et al. 2002, ApJ, 574, 1066
Nindos, A., & Zhang, H. 2002, ApJ, 573, L133
Nindos, A., & Andrews, M. D. 2004, ApJ, 616, L175
Nindos, A., Zhang, J., & Zhang, H. 2003, ApJ, 594, 1033
Phillips, A. D., MacNeice, P. J., & Antiochos, S. K. 2005, ApJ, 624, L129
Priest, E. R., van Ballegooijen, A. A., & Mackay, D. H. 1996, ApJ, 460, 530
Riley, P., Linker, J. A., & Mikić, Z. 2001, J. Geophys. Res., 106, 15889
Romano, P., Contarino, L., & Zuccarello, F. 2003, Sol. Phys., 218, 137
Romano, P., Contarino, L., & Zuccarello, F. 2005, A&A, 433, 683
Steinolfson, R. 1991, ApJ, 382, 677
Sturrock, P. A. 1991, ApJ, 380, 655
Tóth, G. 1996, Astrophys. Lett. & Comm., 34, 245
Usmanov, A. V., Goldstein, M. L., Besser, B. P., & Fritzer, J. M. 2000, J. Geophys. Res., 105, 12675
van Driel-Gesztelyi, L., Démoulin, P., & Mandrini, C. H. 2003, Adv. Space. Res., 32, 1855
Vršnak, B., Ruždjak, D., Sudar, D., & Gopalswamy, N. 2004, A&A, 423, 717
Yang, G., Xu, Y., Cao, W., et al. 2004, ApJ, 617, L151
Yashiro, S., Gopalswamy, N., Michalek, G., et al. 2004, J. Geophys. Res., 109, A07105